Monthly Notices of the ROYAL ASTRONOMICAL SOCIETY

MNRAS **518,** 1789–1801 (2023) https://doi.org/10.1093/mnras/stac3210
Advance Access publication 2022 November 10

What powers the wind from the black hole accretion disc in GRO J1655−40?

Ryota Tomaru [1★] Chris Done [1★] and Junjie Mao [2,3★]

[1] *Centre for Extragalactic Astronomy, Department of Physics, Durham University, South Road, Durham DH1 3LE, UK*
[2] *Department of Physics, Hiroshima University, 1-3-1 Kagamiyama, Higashi-Hiroshima, Hiroshima 739-8526, Japan*
[3] *SRON Netherlands Institute for Space Research, Niels Bohrweg, NL-2333 CA Leiden, the Netherlands*

Accepted 2022 November 3. Received 2022 November 3; in original form 2022 April 16

ABSTRACT

Black hole accretion discs can produce powerful outflowing plasma (disc winds), seen as blue-shifted absorption lines in stellar and supermassive systems. These winds in quasars have an essential role in controlling galaxy formation across cosmic time, but there is no consensus on how these are physically launched. A single unique observation of a stellar-mass black hole GRO J1655−40 was used to argue that magnetic driving was the only viable mechanism and motivated unified models of magnetic winds in both binaries and quasars. The alternative, X-ray heating (thermal-radiative wind), was ruled out for the low observed luminosity by the high wind density estimated from an absorption line of a metastable level of Fe XXII. Here, we reanalyse these data using a photoionization code that includes cascades from radiative excitation as well as collisions in populating the metastable level. The cascade reduces the inferred wind density by more than an order of magnitude. The derived column is also optically thick, so the source is intrinsically more luminous than observed. We show that a thermal-radiative wind model calculated from a radiation hydrodynamic simulation matches well with the data. We revisit the previous magnetic wind solution and show that this is also optically thick, leading to a larger source luminosity. However, unlike the thermal-radiative wind, it struggles to reproduce the overall ion population at the required density. These results remove the requirement for a magnetic wind in these data and remove the basis of the self-similar unified magnetic wind models extrapolated to quasar outflows.

Key words: accretion, accretion discs – black hole physics – line: formation – radiative transfer – X-rays: binaries – X-rays: individual: GRO J1655−40.

1 INTRODUCTION

Black hole accretion flows are generically able to launch winds. These are seen in active galactic nuclei (AGNs), where the mass, momentum, and energy carried by the wind impact the host galaxy, controlling star formation via AGN feedback (Crenshaw, Kraemer & George 2003; Laha et al. 2021). If this wind is magnetic, then it can also contribute to (or even dominate) the angular momentum transport process in the disc. A small amount of material accelerated along the field lines can carry most of the angular momentum outwards, enabling accretion by allowing the rest of the material to fall inwards (Blandford & Payne 1982). Such magnetic winds are scale free, so should be present in the much brighter Galactic binary systems as well as in AGNs.

Winds are seen as blue-shifted absorption features in the Galactic binaries (Ueda et al. 2004; Miller et al. 2006a, b; Miller et al. 2016). However, unlike AGN, where there are multiple other wind launching mechanisms due to their lower disc temperatures, the only competing process in binaries is thermal winds, driven by X-ray heating of gas in the photosphere of the outer disc, or thermal-radiative winds, where radiation pressure gives an additional component to the outwards acceleration. The launch radius of thermal winds is determined by the spectrum of the illuminating radiation. This heats the photosphere to an equilibrium temperature, $T_{\rm IC,7}$, produced by Compton heating/cooling and given in units of 10^7 K. This is independent of radius, while the escape velocity due to gravity decreases as $v_{\rm esc} = 5 \times 10^2\ T_{\rm IC,7}^{0.5}$ km s^{-1}. This means the irradiated gas is unbound for radii above $R_{\rm IC} = 6 \times 10^5/T_{\rm IC,7}\ R_{\rm g}$. This dependence of the wind properties (launch radius/velocity) on the Compton temperature mean that thermal winds respond structurally to changes in the illuminating spectrum, in addition to the predicted change in ionization.

Observationally, winds are only seen in a very specific subset of objects. These all at fairly high inclination angles and have soft (disc-dominated) spectra, with $T_{\rm IC,7} \sim 1$ (Ponti et al. 2012). They have long orbital periods, i.e. large discs as required for the thermal winds at these irradiating temperatures, and the wind velocity is of order 100–1000 km s^{-1} (Díaz Trigo & Boirin 2016), again as predicted by the thermal wind models. This suggests that thermal driving is the main mechanism that produces the observed winds in X-ray binaries.

None the less, radiation driving should also modify the resulting thermal wind structure for $L/L_{\rm Edd} > 0.1$–0.2. This is confirmed by

★ E-mail: ryota.tomaru@durham.ac.uk (RT); chris.done@durham.ac.uk (CD); jmao@tsinghua.edu.cn (JM)

recent radiation hydrodynamics simulations (Tomaru et al. 2019; Higginbottom et al. 2020). These show that including radiation driving in the thermal wind calculations (thermal-radiative winds) is important to get a detailed match to the observations, otherwise the winds seen at high inclination are slower than observed (see also e.g. Luketic et al. 2010; Higginbottom et al. 2014). The radiation force is not just from electron scattering as the wind is not completely ionized close to the disc surface in the disc-dominated soft states, so there is some remaining bound–free (edges) and bound–bound (line) opacity. All three components add together to the total radiation force that helps unbind the material when thermal heating alone is insufficient. Results from these simulations can even match in detail to the observed absorption lines from He and H-like Fe in typical objects (e.g. H1743−322 in Tomaru et al. 2020a and GX 13+1 in Tomaru et al. 2020b).

The simulations also confirm that thermal winds should become invisible when the source makes a transition to the hard state, with $T_{\rm IC,7} \sim 10$. The wind may be launched quite efficiently (though this depends on details of the inner disc geometry) but it is faster, so is less dense. This, together with the harder spectral illumination, means that it is completely ionized so there is no radiation force from bound–bound and bound–free, and these states are typically seen at $L/L_{\rm Edd} < 0.1$ so electron scattering is not important either (Tomaru et al. 2019).

Despite these successes of the thermal-radiative wind models, an alternative mechanism, magnetic driving, is still considered because of a single observation of a very unusual wind in GRO J1655−40. The high-quality X-ray grating spectrum by *Chandra* of GRO J1655−40 during its 2005 outburst shows absorption lines from unusually low ionization states, including a density sensitive metastable absorption line (λ11.92 of B-like Fe XXII). This gives a wind density of (4.0–6.3) $\times$ 10^{13} cm^{-3} (Miller et al. 2008, revised down from the original claim of 5.6 $\times$ 10^{15} cm^{-3} in Miller et al. 2006a). This gives a direct estimate of the launch radius when combined with the observed luminosity, $L \sim 0.04 L_{\rm Edd}$, and ionization parameter $\xi = L/(nR^2) \sim 10^5$ erg cm s^{-1} (Miller et al. 2006a), where n is the number of densities for hydrogen and R is the radius from the source. (In this paper, we use both R and r to show radii. For the model of thermal winds in Section 4, we use R. For the model of magnetic winds in Section 5, we use r. In Section 5, $r_{\rm d}$ shows the radius along the disc mid-plane and r_0 shows the inner radius of this object taken from Fukumura et al. 2017.) The resulting radius is more than a factor of 10 smaller than expected for a thermal wind, *requiring* magnetic launching (Miller et al. 2006a, 2008). By extension, this supported a unified model of magnetic winds across the mass scale, including both stellar and supermassive black holes (Fukumura et al. 2017, hereafter F17).

However, the density derived above assumed that the metastable level is populated only by collisional (electron impact) excitation but photoexcitation can also be important (Mauche, Liedahl & Fournier 2003, 2004). Electrons in the ground level can be photoexcited to upper levels, and de-excite via a radiative cascade that can populate the metastable level. This process is not included in the standard photoionization code used to analyse X-ray data (XSTAR; Kallman & Bautista 2001). Here instead, we use the photoionization code `pion` (Miller et al. 2015; Mehdipour, Kaastra & Kallman 2016; Mao et al. 2017) in the X-ray spectral analysis code SPEX (v3.05; Kaastra et al. 2018) to include these processes and re-assess the density of the photoionized wind in GRO J1655−40 in a self-consistent way. This significantly reduces the inferred density, bringing the launch radius back into the range of thermal-radiative winds. Additionally, the derived column density from this code implies that the wind is optically thick so that the intrinsic luminosity is much larger than the observed luminosity.

We show an explicit optically thick thermal-radiative wind model that gives a good overall match for the wind properties, aligning this critical observation with all other data from binary winds for which the thermal-radiative wind simulations provide a good match (Higginbottom et al. 2019, 2020; Tomaru et al. 2019, 2020a, b).

Our result removes the requirement for magnetic winds in binaries. We also show some specific magnetic wind models, based on the self-similar solutions of F17 and show that these also go optically thick, and cannot easily match even our new lower density, let alone the original density which motivated the magnetic wind models in the first place. This challenges the plausibility of magnetic models to explain these data, and so by extension, the argument for self-similar magnetic winds in AGNs. Instead, this opens the way to a quantitative model for AGN feedback using the known – but complex – physics of ultraviolet (UV) line driving and dust driving in supermassive black hole accretion flows.

2 OBSERVATIONAL DATA

GRO J1655−40 is a well-studied Galactic low-mass X-ray binary (Hjellming & Rupen 1995; Orosz et al. 1997; Abramowicz & Kluźniak 2001), whose distance is $d \sim 3.2$ kpc (Hjellming & Rupen 1995), orbital period is 2.6 d (Greene, Bailyn & Orosz 2001), and black hole mass is $M_{\rm BH} = 5.4 \pm 0.3$ M$_\odot$ while the companion star has mass $M_{\rm s} = 1.45 \pm 0.35$ M$_\odot$ (Beer & Podsiadlowski 2002). The orbital period and the masses give an outer disc radius of $R_{\rm out} = 4 \times 10^{11}$ cm $= 5 \times 10^5$ $R_{\rm g}$, where $R_{\rm g} = GM_{\rm BH}/c^2$ assuming that the outer disc extends to 80 per cent of the Roche lobe radius.

During the outburst in 2005, this object showed an unusual continuum shape called a hyper-soft state (Neilsen et al. 2016). This is accompanied by unusual absorption line features from low-ionization ion species (e.g. Li-, Be-, and B-like Fe ions) observed with the high-energy grating (HEG) aboard the *Chandra* X-ray Observatory. None of the other observations of black hole binaries shows these absorption lines (Miller et al. 2006a, 2008).

We take these data (ObsID: 5461) on 2005 April 1 (i.e. Modified Julian Date = 53461) from the Chandra Transmission Grating Data Catalog and Archive (TGCat; Huenemoerder et al. 2011). Similar to previous works (Miller et al. 2008; Kallman et al. 2009), the positive and negative first-order HEG data were combined using CIAO v4.13 (Fruscione et al. 2006). In addition, the spectral data and response files are converted into SPEX formats using *trafo*.

3 PHOTOIONIZATION MODELLING OF THE HIGH-RESOLUTION X-RAY SPECTRUM

We reanalyse the *Chandra*/HEG spectrum using the photoionization model `pion` in SPEX (v3.05; Kaastra et al. 2018). Compared with the alternative photoionization modelling using XSTAR (Kallman & Bautista 2001), the advantage of `pion` is that it can track the multiple radiative decay pathways that can populate the metastable levels (Mao et al. 2017). Additionally, it includes electron scattering (Kastner 1993) as well as atomic absorption in determining the observed continuum flux, and calculates on the fly the ion populations in spectral fitting self-consistently from the full SED model. Fig. 1 shows our fitting to the *Chandra*/HEG spectrum.

We first explore the overall SED/absorber properties using the *Chandra*/HEG data alone (black points in Fig. 2a). We use a single Comptonization model as the continuum, with two `pion` absorbers

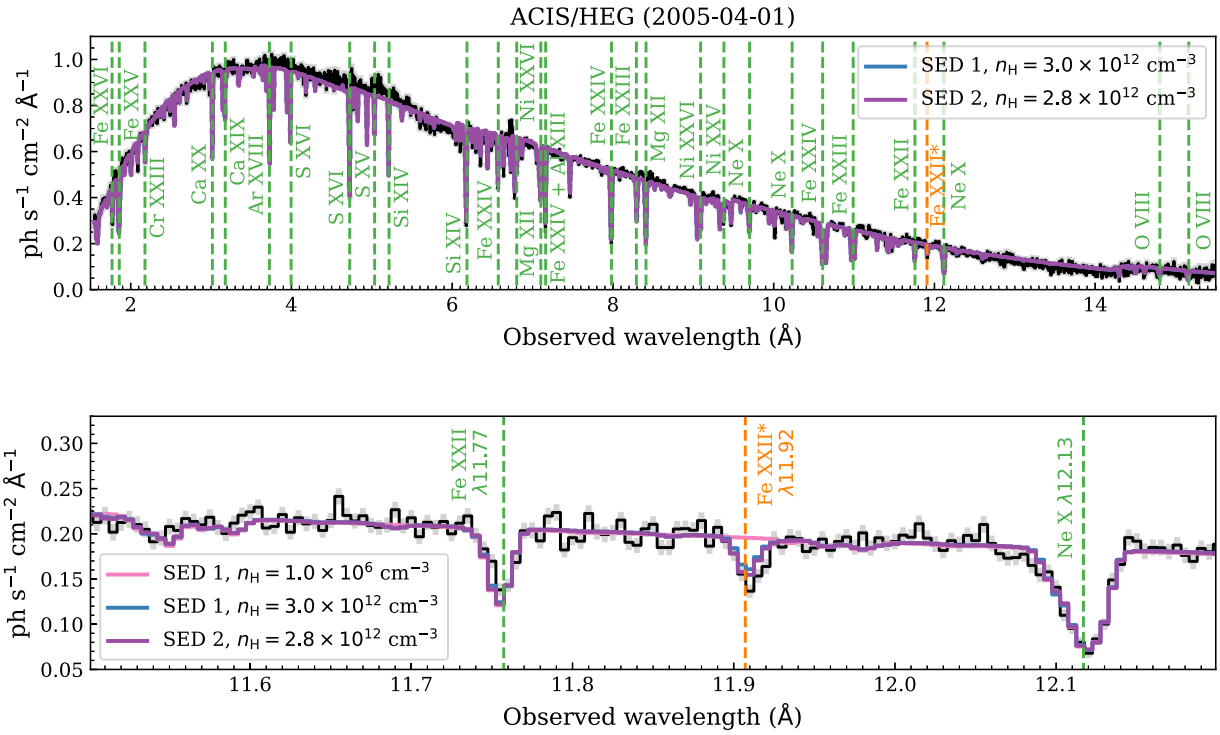

Figure 1. Photoionization modelling to the Chandra grating spectrum of GRO J1655−40. Results from two distinct spectral energy distributions (SEDs) are shown (overlapped) with barely visible differences. The bottom panel zooms in to show the Fe XXII and Fe XXIII absorption lines." The colours show absorption lines from ground (green) and metastable (orange) levels. A low-density model (pink) cannot produce the observed metastable absorption lines.

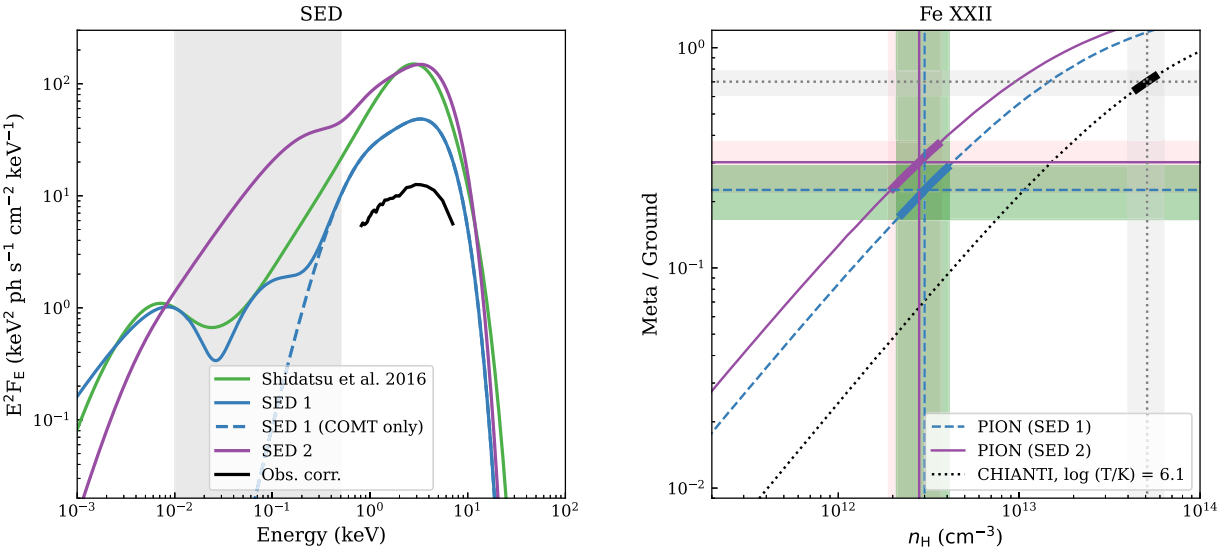

Figure 2. *Left:* The spectral energy distributions SED-1 (blue) and SED-27 (purple) used in this work compared to that inferred by (Shidatsu, Done & Ueda 2016) (green). The black curve is the observed Chandra grating spectrum corrected for Galactic absorption and smoothed to show the continuum level. The shaded area in grey corresponds to 0.01–0.5 keV where no observable data are available to constrain the SEDs. *Right:* This shows the metastable to ground level population ratios for Fe XXII for SED-1 (blue) and SED-2 (purple) compared to that for collisional ionized equilibrium (black) processes alone. The latter was calculated using CHIANTI v10.0.1 (Del Zanna et al. 2021). Increasing the intrinsic soft X-ray flux decreases the required density. It also increases the optical depth of the ground level transition at λ11.77 ($2s^2\ 2p\ ^2P_{1/2}$). This means the line is more saturated, so its observed equivalent with does not increase linearly with the level population, so this also reduces the metastable (λ11.92: $2s^2\ 2p\ ^2P_{3/2}$) to ground level ratio from that given simply from the ratio of their observed equivalent widths and oscillator strengths.

partially covering the source (see also, Miller et al. 2008; Kallman et al. 2009).

Most of the observed absorption lines arise from the lower ionization zone, which has a line of sight hydrogen column density of $\sim 5 \times 10^{23}$ cm^{-2}, covering 60 per cent of the source, similar to previous analyses. The higher ionization zone contributes most to the H- and He-like lines, especially Fe XXV and Fe XXVI. This zone covers most of the source, is faster, and has column density that is optically thick to electron scattering, such that the intrinsic luminosity at 1–10 keV is a factor $\sim$3 larger than the observed luminosity. Previous studies fit only to the ion columns, and did not include the effect of electron scattering in attenuating the illuminating flux. Thus the derived intrinsic SED (dashed blue line in Fig. 2a) is higher than observed (black) data.

The low-ionization zone produces the Fe XXII λ11.92 metastable line. This is the first excited state above the ground, so can be populated by free electrons colliding with the ground state ion, raising the outer electron to this level. However, it can also be populated from above as a result of radiative cascades of electrons in higher excited levels. The upper levels which can most efficiently radiatively decay down to the metastable level are those with the 2s 2p^2 configuration. These are excited by photons with $h\nu \sim 0.1$ keV. Mauche et al. (2003) say these are faint in their particular object, an accreting white dwarf, so that this process can be neglected, but our object is a black hole accretion disc, which is likely bright at these energies.

We cannot directly observe the SED at 0.1 keV due to interstellar absorption, which makes the grey-shaded area in Fig. 2(a) unobservable. We cannot even uniquely know the 1–10 keV X-ray luminosity due to electron scattering in the optically thick absorber. Hence, we consider a range of different SED shapes and luminosities to span a plausible range of ionising continua for our analysis. The green line in Fig. 2(a) is an SED derived by Shidatsu et al. (2016), where the optical and UV flux match the observed level, but the X-rays are much brighter due to their even higher assumed electron scattering optical depth of $\tau \sim 3$. We add components to our Comptonization continuum to make it resemble the shape of the SED of Shidatsu et al. (2016) below 0.1 keV. This is shown as the solid blue line in Fig. 2(a), SED-1.

There could be much more flux at 0.1 keV if the intrinsic luminosity derived by Shidatsu et al. (2016) is correct. We match the Comptonized continuum to their 1–10 keV luminosity, and add the maximum disc continuum that is allowed by the contemporaneous UV data from *Swift*/UVOT. This SED-2 is shown as the purple line in Fig. 2(a). Compared to SED-1, the 1–10 keV intrinsic flux of SED-2 is higher, which is favoured by Neilsen et al. (2016), Shidatsu et al. (2016), and Higginbottom et al. (2018). More importantly for our study, SED-2 has more than an order of magnitude more flux at 0.1 keV relative to the 1–10 keV flux than SED-1.

We fit the data with both SEDs. The high-ionization absorber should be closest to the source, so it filters the continuum seen by the lower ionization absorber. The lower ionization absorber (where the metastable lines are produced) is not optically thick, so the transmitted continuum that illuminates this zone must be around the level of the observed continuum. SED-1 gives results that are very similar to the initial fits with just a single Comptonization component as the SED, with an optical depth of $\sim$2 (column density of $\sim 2.5 \times 10^{24}$ cm^{-2}) so that the observed luminosity is a factor $\sim$3 smaller than the intrinsic when the covering fraction is taken into account. The higher luminosity of SED-2 requires a combination of a higher column density and a higher covering fraction in order to sufficiently attenuate the flux, but gives a similarly good fit to the data as the lines are highly saturated (Table 1).

Table 1. Best-fitting parameters of *Chandra* HEG spectrum of GRO J1655−40 observed on 2005 April 1. Expected *C*-statistics are calculated as described in Kaastra (2017). Frozen parameters are indicated with (f). All quoted errors refer to statistical uncertainties at the 68.3 per cent confidence level.

Model	SED 1	SED 2
	Statistics	
$C_{\rm stat}$	12 587.0	12 651.1
$C_{\rm expt}$	2793 ± 75	2793 ± 75
d.o.f.	2775	2776
	Galactic absorption	
$N_{\rm H}$ (10^{21} cm^{-2})	5.55 ± 0.07	5.61 ± 0.02
	Comptonization	
Norm (ph s^{-1} keV^{-1})	$7.8^{+0.2}_{-2.6} \times 10^{46}$	$24.0^{+1.1}_{-3.6} \times 10^{46}$
$T_{\rm seed}$ (keV)	0.192 ± 0.004	0.193 (f)
$T_{\rm plasma}$ (keV)	1.109 ± 0.003	1.111 ± 0.002
τ	12.68 ± 0.07	12.60 ± 0.09
	pion #1	
$N_{\rm H}$ (cm^{-2})	$2.49^{+0.04}_{-0.73} \times 10^{24}$	$4.27^{+0.10}_{-0.14} \times 10^{24}$
$\log \xi$ (erg s^{-1} cm)	3.90 ± 0.01	4.09 ± 0.01
$f_{\rm cov}$	$0.77^{+0.01}_{-0.10}$	0.92 ± 0.06
$v_{\rm out}$ (km s^{-1})	-598 ± 16	-621 ± 10
$v_{\rm mic}$ (km s^{-1})	143 ± 7	145 ± 4
	pion #2	
$N_{\rm H}$ (cm^{-2})	$(4.7 \pm 0.4) \times 10^{23}$	$(4.7 \pm 0.3) \times 10^{23}$
$\log \xi$ (erg s^{-1} cm)	3.38 ± 0.02	3.44 ± 0.15
$f_{\rm cov}$	0.57 ± 0.02	0.59 ± 0.01
$n_{\rm H}$ (cm^{-3})	$(3.0 \pm 0.5) \times 10^{12}$	$(2.8 \pm 0.4) \times 10^{12}$
$v_{\rm out}$ (km s^{-1})	-310 ± 12	-323 ± 3
$v_{\rm mic}$ (km s^{-1})	93 ± 3	99 ± 2

The main density diagnostic line is from the ratio of the Fe XXII metastable line (11.92 Å) to the ground level resonance line (11.77 Å). The black line in Fig. 2(b) shows the density derived from only collisional ionization. In this solution, the ground state line is not strongly saturated, so the ratio of the observed equivalent width between the metastable and ground state directly estimates the ratio of level populations. The blue and magenta lines show the results of SED-1 and SED-2, respectively. Radiative cascades from excited states in both SEDs shift the derived density to $n_{\rm H} = (2.8 \pm 0.9) \times 10^{12}$ cm^{-3}, down by over an order of magnitude from those reported previously (Miller et al. 2008). These SEDs also shift the inferred level population ratio down from that directly measured from the ratio of equivalent widths as the ground level line becomes optically thick (optical depth $\tau \sim 3.5$–4 in both SEDs).

The decrease in density, together with the increased intrinsic luminosity, dramatically changes the inferred wind launch radius to be $\sim 10^{11}$ cm. By comparison, the Compton temperature for both SEDs is $\sim 6.4 \times 10^6$ K, giving a Compton radius $R_{\rm IC} \sim 8.4 \times 10^{11}$ cm. Thermal winds can be launched from 0.1 to 0.2 $R_{\rm IC}$ (Woods et al. 1996), clearly compatible with the new launch radius derived above.

4 A SPECIFIC THERMAL-RADIATIVE WIND MODEL

We build a spectral model based on two-dimensional radiation hydrodynamic calculations of a thermal-radiative wind to compare to the observed spectrum by *Chandra*. We use the same radiation

hydrodynamic simulation code as Tomaru et al. (2019, 2020b). The code takes as input the broad-band X-ray continuum from the central source, its luminosity and a disc size, and can calculate the dynamics of the gas ionized, heated, and accelerated by that radiation. This radiation heating/cooling includes the line process (bound–bound), as well as bound–free, free–free, and Compton processes. The radiative acceleration includes bound–bound, bound–free, and electron scattering. These effects are pre-calculated by CLOUDY (Ferland 2003) and converted to a look-up table as a function of ionization parameter ξ and temperature T for the radiation hydrodynamic simulation.

The previous section has shown the difficulty in determining the intrinsic SED shape and luminosity. We take a single spectrum which is roughly the geometric mean of SED-1 and SED-2 in the X-ray bandpass (shown in the left-hand panel in Fig. A1) with luminosity $L = 0.5L_{\rm Edd}$. The corresponding Compton temperature that is the equilibrium temperature at highest ionization parameter is $T_{\rm IC} = 7.6 \times 10^6$ K. The thermal equilibrium curve of photoionized gas irradiated by that SED is shown the right-hand panel of Fig. A1. Our simulation calculates the time evolution of gas on the disc surface that is illuminated by this SED.

In our simulation, we use a time-dependent boundary condition on the disc surface, where the pressure ionization parameter $\Xi = \Xi_c = L\exp(-\tau)/(4\pi R^2 cnkT)$ takes a constant critical value in order to set the base density of the wind. Here, τ is defined as the total optical depth of the wind and inner corona (atmosphere) along the line of sight from the centre to the disc surface, and Ξ_c is set by the first thermal instability point, where the photoionized plasma makes a transition from a hot to cooler phase. The value of Ξ_c depends on the shape of the irradiating spectrum (see Appendix A). We use the first instability point to set Ξ_c since the cold gas becomes optically thick quickly due to line and bound-free opacity and the reprocessed emission is also important. However, we calculate this point assuming that the gas is optically thin, which means that the spectral shape is not different by that attenuation. We will explore this effect in more detail using the realistic transmitted spectrum in a future work to show how different that is to the completely optically thin thermal winds with different boundary conditions (Luketic et al. 2010; Dyda et al. 2017).

Fig. 3 shows the ion column densities and average velocity of each ion as a function of angle through the simulated wind structure (Fig. A3). At high inclination angle, the hydrogen column density is optically thick with $N_{\rm H} \sim 10^{24}$ cm^{-2}. At inclination angle $\theta = 78$–81° ($\cos\theta = 0.15$–0.2), the Fe XXII columns show the almost same value as required for the ground state 11.77 Å line ($N_{\rm xxii} = 1.9 \pm 0.1 \times 10^{16}$ cm^{-2}; Miller et al. 2008). The velocity at these angles is also the same as observed.

We calculate transmitted spectra for the high inclination angle region (75–85°) of this wind using the XSTAR (Kallman & Bautista 2001). In this calculation, we do not include any artificial turbulent velocity to give additional broadening of the lines. We build a multiplicative tabular model (`mtable`) in XSPEC and fit the data as $mtable$(RHDwind) × ($ezdiskbb + nthcomp$) with Galactic absorption. The best-fitting parameter is 80° and this transmitted spectrum matches fairly well to the observed data in terms of the ion states seen (Fig. 4). One major exception is the absorption line from the metastable level of Fe XXII, but this is due to our use of XSTAR, which does not include the radiation cascade populating this level. Additional mismatches are in the Fe XXV line, which may indicate there is significant emission from the wind in this line, and in the Ne X line at 11.23 Å, which is probably due to the rather low abundance of Neon assumed in XSTAR. (The default is 2.8×10^{-5} relative to hydrogen compared to e.g. 1.2×10^{-4} reported in Lodders, Palme & Gail 2009, which is default abundance of SPEX.)

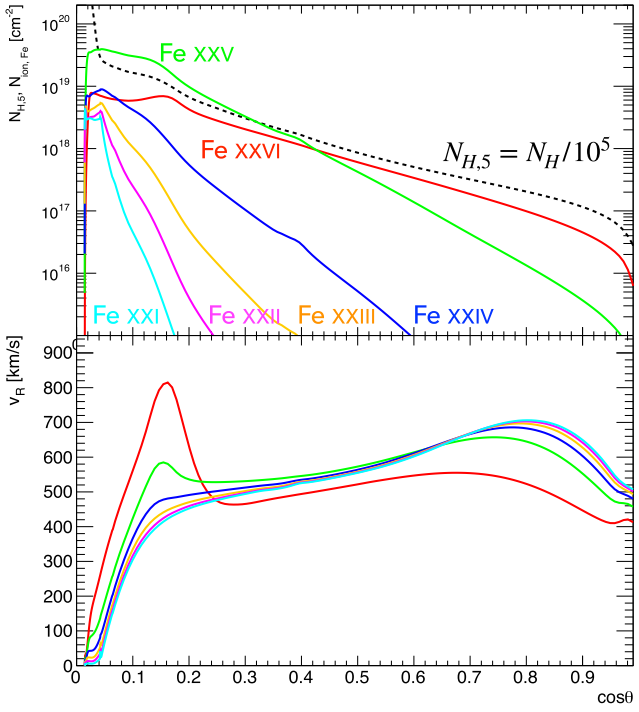

Figure 3. The inclination dependence of the hydrogen column density and Fe ion columns (top), and average velocity weighted by those ion columns (bottom) for the thermal-radiative wind model. Colours show Fe XXVI (red), XXV (green), XXIV (blue), XXIII (yellow), XXII (magenta), and XXI (cyan).

The density of our wind in the region where Fe XXII is produced is similar (within a factor of 2) to that required from the `pion` analysis (see Fig. 5). The overall optical depth to electron scattering along this sightline ($\cos\theta = 0.15$) is $\tau_{\rm es} \sim 1.0$ (Fig. 3), a factor of 2 lower than that required to attenuate the intrinsic luminosity down to the level observed. Both these order 2 mismatches are likely due to the additional illumination of the outer disc by scattered flux in the wind that is not included in our radiative hydrodynamics code. This will increase the density of the wind and hence decrease the observed flux. None the less, even without scattering, the thermal-radiative wind simulation shows a good overall match to the observed absorption structure. The wind density (dotted grey line in Fig. 5) drops as $\sim R^{-1}$ over an order of magnitude change in radius, from $(0.1$–$1)R_{\rm out} = (0.05 - 0.5)R_{\rm IC}$.

This strongly contrasts with the expectations of optically thin thermal winds as $n \propto R^{-2}$ at high inclination angles (Luketic et al. 2010). These are the result of the base wind density of $n_0(R) \propto R^{-2}$ is set by the thermal instability via Ξ_c with optically thin limit ($\tau = 0$).

Hence, the luminosity ionization parameter $\xi = L/nR^2$ is constant, which is quite unlike the wind seen in these data. Instead, in our optically thick thermal-radiative wind, there is a wide range in ionization parameter in the wind, with high-ionization material (Fe XXVII: black and XXVI: red) located at smaller radii while Fe XXII (magenta) peaks towards the outer disc radius. This gives a higher line-of-sight velocity (dashed line) for the higher ionization ion states, as observed.

Thus, the results of this single radiation hydrodynamic simulation of an optically thick thermal-radiative wind give a good overall match to all the observed features, both the density derived from the metastable level of Fe XXII and the range of ion species seen, and

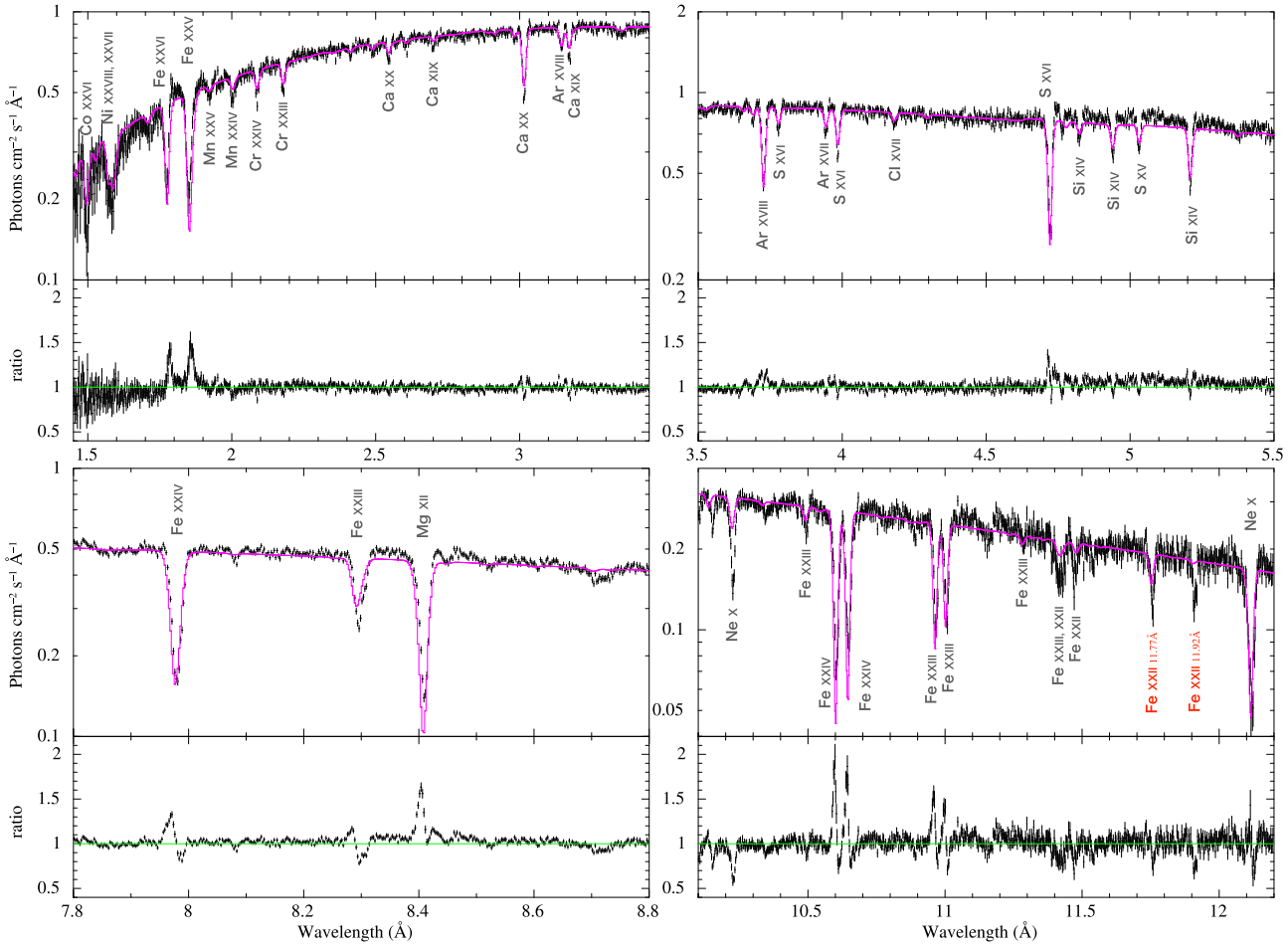

Figure 4. The *Chandra*/HEG spectrum of GRO J1655−40 (black) compared to the thermal-radiative wind model (magenta). We use the same energy range as Fukumura et al. (2017) for comparison easily. The model is calculated by radiation transfer via XSTAR though the best-fitting line of sight. The continuum shape is the only additional free parameter, but its value is within a factor of ∼4 of the observed luminosity.

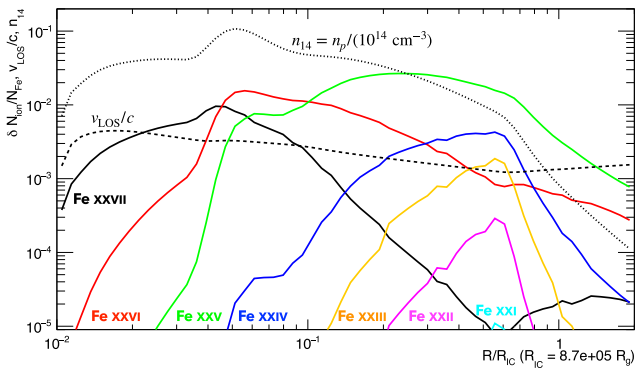

Figure 5. The radial properties of the optically thick thermal-radiative wind model. The hydrogen density (in units of 10^{14} cm^{-3}; grey dotted line) is almost constant above the disc, then drops sharply beyond the outer disc radius of $R = 4 \times 10^{11}$ cm ($0.5R_{IC}$). The local ion column densities divided by the total iron column density (solid coloured lines) show that the species are stratified, with highly ionized ions produced at smaller radii and Fe XXII peaking at the outer disc radius, where the density is $n = 1.0 \times 10^{12}$ cm^{-3}. The radial velocity (in units of light speed; black dashed line) is also stratified, being ∼300 km s^{-1} for Fe XXII and ∼500 km s^{-1} for Fe XXVI, close to that observed.

to their observed velocities. This shows that thermal-radiative winds are not excluded by this unique observation of GRO J1655−40, and in fact given that there no real free parameters barring the inclination, this proof of concept calculation gives strong evidence in favour of an optically thick, thermal-radiative wind as the explanation of these data. However, given the interest in magnetic winds in the literature, we revisit the magnetic wind solutions and compare the results of these models to our thermal-radiative wind solution.

5 THE F17 MAGNETIC WIND MODEL FOR GRO J1655−40

Current magnetic wind models use an ordered, large-scale field threading the disc and rotating with it, and assume self-similar behaviour (Fukumura et al. 2010; Chakravorty, Lee & Neilsen 2013). In the models of F17 (based on previous work of Blandford & Payne 1982; Contopoulos & Lovelace 1994), the field line geometry required is solved self-consistently with the assumed power-law radial density profile of the wind at its streamline base on the disc surface at radius r_d such that $n(r_d) = n(r_0)(r_d/r_0)^{-q}$, where r_0 is the inner radius of the disc ($r_0 = 3.81 \times 10^6$ cm for GRO J1655−40). In this approach, the wind density can be arbitrarily high.

F17 used an older version of XSTAR (v2.2.1bn21), but this did not include the atomic data for the critical Fe XXII lines at 11.77 and

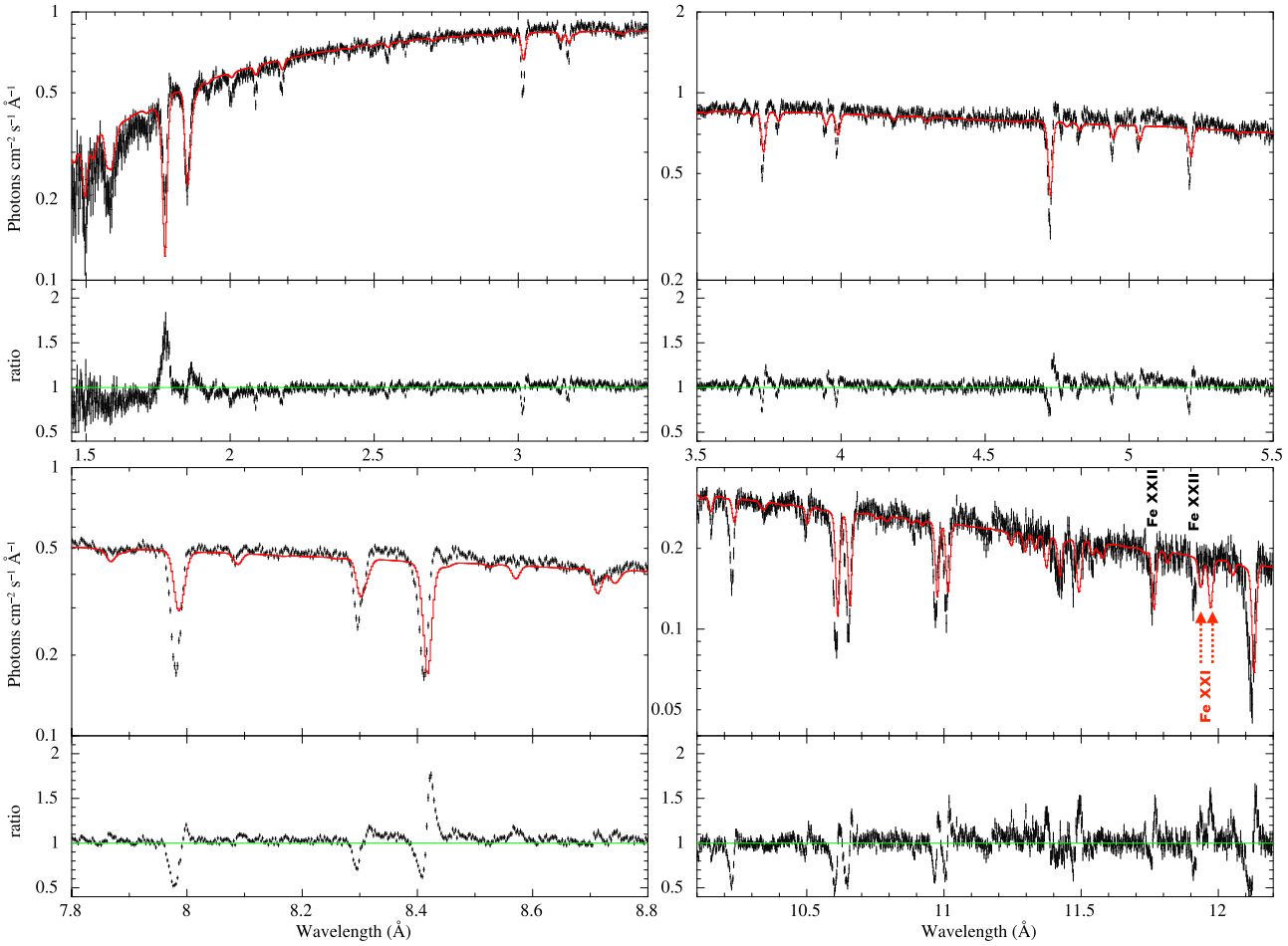

Figure 6. Our version of the MHD wind model of F17, i.e. with density $n(r_{\rm sp}, 80^\circ) = 1.4 \times 10^{17}(r_{\rm sp}/r_0)^{-1.2}$ cm^{-3}. The overall fit quality is similar to that shown in F17 across the range of ion states seen.

11.92 Å. We recompute the magnetic wind model F17 designed to fit GRO J1655−40 using updated version of XSTAR (v2.58e).

We calculate an MHD wind solution for these data using the density profile of F17 where $n(r, \theta) = n_0(r/r_0)^{-1.2}\exp[5(\theta - \pi/2)]$. F17 state that they use $n_0 = 9.3 \times 10^{17}$, $\theta = 80^\circ$, i.e. $n(r, 80^\circ) = 3.9 \times 10^{17}(r/r_0)^{-1.2}$ as the best fit for the broad-band spectrum of *Chandra*/HEG but there were hidden overall scaling factors in their models. The actual density used is not easy to recover but may be around $n_0 = 3.5 \times 10^{17}$ cm^{-3}, so that the corresponding density profile at $\theta = 80^\circ$ is $n(r, \theta) = 1.4 \times 10^{17}(r/r_0)^{-1.2}$ (Fukumura, private communication). The ionization parameter is then $\xi = L/(nr^2) = 2.4 \times 10^7(r/r_0)^{-0.8}$ erg cm s^{-1}.

We first calculate the absorption over the radial range of $r_0 - 10^6 r_0$ at 80° as used in F17, but note that this gives an outer disc radius of 3.81×10^{12} cm, almost an order of magnitude larger than the expected outer radius of the disc in this system of 4.4×10^{11} cm. We also use the observed luminosity as the intrinsic luminosity as in F17 ($L = 5.0 \times 10^{37}$ erg s^{-1}). We split the column into 64 bins of equal logarithmic size in $\delta r/r$. The radial velocity along the line of sight for a streamline is $v_r(r, 80^\circ)/c = 0.17(r/r_0)^{-0.5} \sim \cos 80^\circ (r/r_0)^{-0.5}$, i.e. the wind has slow radial outflow velocity in the equatorial plane [most of its velocity is in the azimuthal direction, at the Keplerian velocity, $v_\phi(r)$], and is radially accelerated by magneto-centrifugal forces. Using these parameters, we solve for the radiation transfer along line of sight by chaining XSTAR. We calculate the transmitted spectra in the rest frame of the each wind element and the previous transmitted spectrum is used as next input spectrum.

Fig. 6 shows the resulting fit to the *Chandra*/HEG data, where the model has additionally been Gaussian smoothed to the instrument resolution using the `gsmooth` model in XSPEC. We mark the positions of the Fe XXII density diagnostic lines at 11.77 and 11.92 Å. The older version of XSTAR used by F17 did not include these lines so has no contribution from either of these lines. The newer XSTAR version used in our calculation does include these absorption lines, but only includes collisional processes to populate the metastable level. The density in this MHD wind model is too small to make the metastable line by only collisional processes despite the wind model being motivated by this feature.

The absorption lines seen at 11.937 and at 11.975 Å are instead from Fe XXI (these transitions were again not included in the version of XSTAR used in F17).

Fig. 7 shows the radial structure of the wind along the 80° of the outer region of the wind, where the most of absorption lines are created. The inner region is completely ionized so has no line absorption. The wind only starts to become observable for $r/r_0 > 10^3$, where H-like iron (Fe XXVI, red line) is able to form, followed by He-like (Fe XXV, green line). The Fe XXII (B-like, magenta line) that produces the density diagnostic line peaks at the outer edge, where the ionization parameter is $\xi = 2.4 \times 10^7(10^6)^{-0.8} \sim 500$ erg cm s^{-1}. The density here is $\sim 10^{10}$ cm^{-3}, which is too low to form the metastable

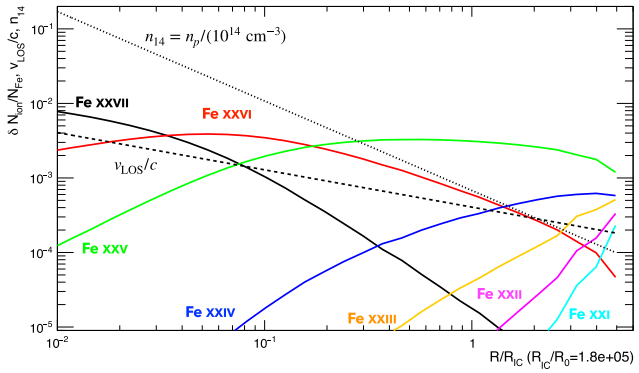

Figure 7. The radial dependence of the local fractional ion column along the 80° line of sight for our version of the magnetic wind model of F17 is shown in Fig. 6. Colours show Fe XXVII (black), XXVI (red), XXV (green), XXIV (blue), XXIII (yellow), XXII (magenta), and XXI (cyan). Fe XXII and Fe XXI are produced close to the outer radius of the wind. The dashed line shows the ratio of the radial velocity to the speed of light and the dotted line shows the hydrogen density normalized by 10^{14} cm^{-3}. This figure only shows the outer region of the wind, where most of absorption lines are created.

level even at the density suggested by our `pion` analysis, let alone the density required for only collisional excitation.

Increasing the density is not in itself a good solution. We tried a model with $n(r, 80^\circ) = 3 \times 10^{17}(r/r_0)^{-1.2}$ but this dramatically increases the low-ionization species such as Fe XXI, strongly over-producing the 11.937 and 11.975 Å absorption lines which are not in the data, as well as predicting multiple other unseen transitions from Fe XXII and XVII to the right and left of the observed Fe XXII lines at 11.427 and 11.491 Å (left, Fig. 8). The observed lack of these additional Fe XXII/XVIII lines (which were not included in the version of XSTAR used by F17) clearly limit the contribution of the lower ionization states of iron, and hence the amount of material with $\xi \gtrsim 500$. The ionization parameter of this MHD wind monotonically decrease with radius, thus this lower limit of ionization parameter must be at the maximum radius of the wind.

Using realistic outer radius $R_{\rm out} = 4.4 \times 10^{11}$ cm as the maximum radius of the wind, which is almost 10 time smaller than that of F17, can give a wind with both higher ionization parameter and higher density. However, the density still lower than the observational value. We show the spectrum at $r = 10^5 r_0$ (right in Fig. 8) with $n(r, 80^\circ) = 3 \times 10^{17}(r/r_0)^{-1.2}$. This spectrum well describes the lower energy band without lines from Fe XXI, but the density at $r = 10^5 r_0$ is 3×10^{11}cm^{-3}, which is still at least 10 times smaller than our derived density with the radiative cascades, and 100 times smaller than for collisional ionization alone. We consider what condition can satisfy the observed density $n = 3 \times 10^{12}$ cm^{-3}, the ionization parameter $500 < \xi < 5000$ (this upper limit is taken from pion analysis), and the observed luminosity $L = 5 \times 10^{37}$ erg s^{-3} using the same density profile as $n \propto (r/r_0)^{-1.2}$. These equation give us the strong constrain of the radius where the Fe XXII is dominant, and it is required to be $5.8 \times 10^{10} = 1.5 \times 10^4 r_0 < r_{\rm xxii} < 1.8 \times 10^{11}$ cm $= 4.7 \times 10^4 r_0$. This also gives us a boundary condition on the density at $r = r_0$ of $3.1 \times 10^{17} < n_{0,80} < 12 \times 10^{17}$ cm^{-3}.

Such a large density means that the model is not self consistent as this wind goes optically thick to electron scattering. This was not included in the models of F17, though the optical depth in their original model is also high, with $\tau_{\rm es} = \sigma_T \int_{r_0}^{r_{\rm out}} n(r, 80^\circ) {\rm d}r = \sigma_T \int_{r_0}^{r_{\rm out}} 1.4 \times 10^{17}(r/r_0)^{-1.2}\,{\rm d}r = 1.7$ Thus, even original model F17 requires $\exp(1.7) = 5.5$ times larger luminosity. Fig. 9 shows the effect of this attenuation on the ionization parameter. At the edge of the outer radius, the ionization parameter is 5.5 times smaller so the ion calculations are not self consistent in F17. Our limits on the MHD inner wind density of $3 \times 10^{17} < n_{0,80} < 12 \times 10^{17}$, give corresponding optical depth of $3.4 < \tau_{\rm es} < 13$. This implies an extremely large intrinsic luminosity ($1.5 \times 10^{39} < L < 2.2 \times 10^{43}$) is required.

The only way(s) to recover a self-consistent solution with the observed density, ionization parameter, and the observed luminosity with the radial dependence $n \propto (r/r_0)^{-1.2}$ is (are) that the intrinsic source luminosity is much larger and/or that the wind only starts from some radius $r \gg r_0$. For example, the column density in the observed (not completely ionized) ion species must be $\geq 5 \times 10^{23}$ cm^{-2}, corresponding to an optical depth of ≥ 0.3. This requires that the wind only starts from a radius of $3 \times 10^4 r_0$ and that the intrinsic luminosity is $L_{\rm obs}\exp(\tau) = 7 \times 10^{37}$ erg s^{-1}. Alternatively, the wind has optical depth 1(3) if it extends down to $5 \times 10^3 r_0$ ($225 r_0$), so the intrinsic luminosity is $\sim 10^{38}(10^{39})$ erg s^{-1}.

Thus even the magnetic wind models have multiple issues with matching the data from GRO J1655−40. The type of solutions proposed in F17 can give a good overall fit to the range of ion states seen for a line-of-sight density $n_{\rm LOS}(r) = 1.4 \times 10^{17}(r/r_0)^{-1.2}$, but this goes extremely optically thick for a wind extending from r_0 to $r_{\rm out}$ as predicted for self-similar winds.

Thus even the MHD wind solutions require that the wind goes optically thick, so the source is intrinsically more luminous than observed. The previous MHD wind solutions did not include the effect of electron scattering on the ionising flux, so their ion populations are not self consistent. We show that including this means that the MHD winds have great difficulty in matching the observed density diagnostic lines, which is ironic as this feature was the motivation for the magnetic wind solutions.

6 DISTINGUISHING MAGNETIC AND THERMAL WIND MODELS FROM LINE PROFILES IN OPTICALLY THIN WINDS

We have shown for the first time that the thermal-radiative wind models can plausibly fit the iconic *Chandra*/HEG data set for GRO J1655−40, not just the broad range of ion species but even the specific metastable level, which was used to rule out the thermal wind models and motivate the MHD models. We also show for the first time that the MHD winds are not self-consistent in their neglect of electron scattering and cannot match the specific metastable level, which was their initial motivator.

Nonetheless, the thermal-radiative wind models also have some issues for these GRO J1655−40 data. They only predict a column density of $\tau \sim 1$, which is not enough to reduce the assumed X-ray flux down to that observed, and the best-fitting inclination angle is much higher than expected from the binary orbit. Plausibly, this is due to our neglect of flux scattering in the wind giving an extra irradiation source for the disc, but this is currently beyond the scope of our codes.

Hence it could be argued that both models (MHD and thermal-radiative) give some mismatch with observations, so it is important to try to find a model-independent way to distinguish the difference between them. Future X-ray spectrometers such as *XRISM*/Resolve and *Athena*/XIFU will give much higher resolution data showing the detailed line profile, so here we explore whether this can give a clean diagnostic of the wind launching mechanism.

Fig. 10 shows a simulation of the expected *XRISM* spectra from the MHD (red) and thermal-radiative (black) wind models, assuming

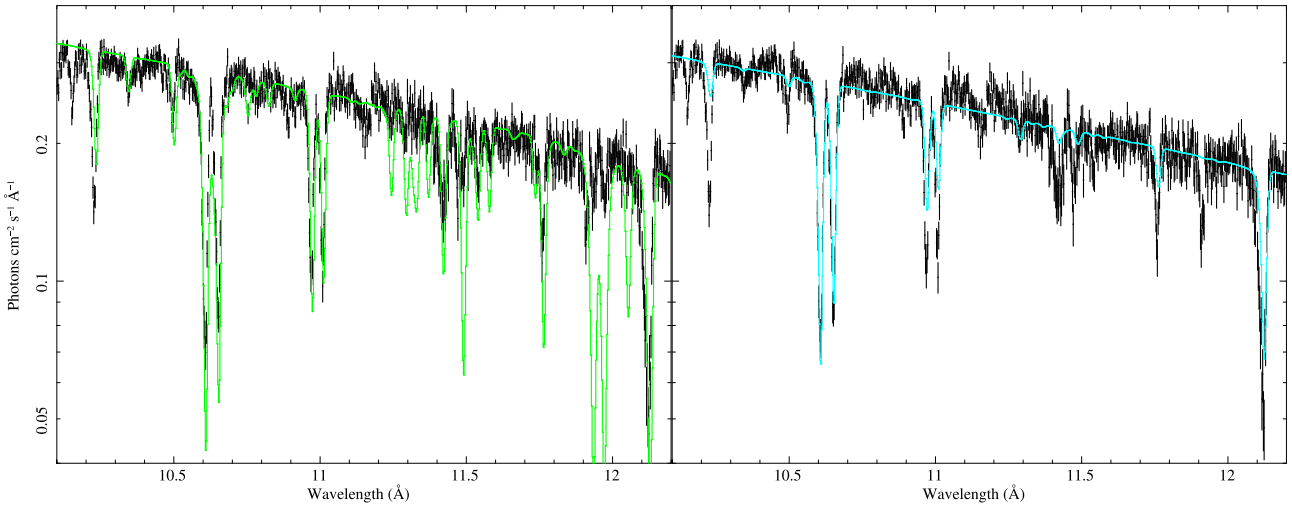

Figure 8. The same figure as F17 for the 10–12.2 Å region but different initial density $n = 3.0 \times 10^{17}(R/R_0)^{-1.2}$ at 80°. Colours show different outer radius with $10^6 R_0$ (green) and $10^5 R_0$ (cyan).

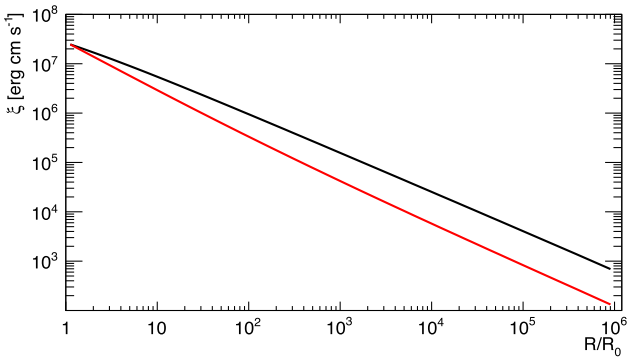

Figure 9. The radial distribution of ionization parameter ξ for the MHD wind model. Colours show optically thin limit (black) and with an attenuation factor $\exp(-\tau)$ (red).

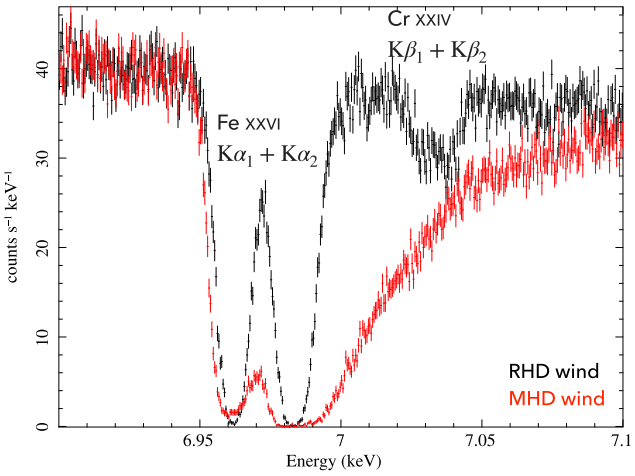

Figure 10. The simulation of observation by the microcalorimeter of *XRISM* with 30 ks for the thermal-radiative wind model (black) and the MHD wind model (red).

the same exposure time as the that of *Chandra*/HEG (30 ks). We pick the Fe XXVI $K\alpha_{1,2}$ line region as this doublet is in a relatively clean part of the spectrum.

The MHD wind (red) shows a strong blue wing as in these models Fe XXVI is produced over a large range in radii, and hence spans a large range in velocity as the MHD wind velocity is $\propto r^{-1/2}$. Higher velocity material also has higher velocity range in a given $d\log r$ segment, so the lines are broader as well as more blueshifted, so are less deep for constant column. Thus the blue wing on MHD winds is a generic feature.

By contrast, the thermal-radiative wind model gives an Fe XXVI line which is relatively narrow and symmetric as the wind velocity produced by thermal heating is relatively constant (Fig. 5). This constant velocity is a fairly generic feature of thermal winds, unless the wind launch radius is of order the disc size (Tomaru et al. 2020a). The low-velocity shear means that the resonance lines are very optically thick, so much weaker lines can contribute to the spectrum. The thermal-radiative wind predicts a noticeable contribution from the Cr XXIV $K\beta_{1,2}$. Interestingly, the third-order *Chandra* spectrum, which is the best resolution so far, has tentative evidence for a feature at this energy, though it was interpreted by Miller et al. (2015) as evidence for a separate velocity component in Fe XXVI $K\alpha_{1,2}$.

Given that the wind in GRO J1655−40 appears to be more optically thick than our thermal-radiative wind simulation, we expect that the line profile in the GRO J1655−40 data would be more complex than that shown here. However, the line of sight through the wind in GX 13+1 is probably comparable to this simulation (Tomaru et al. 2020b), so an observation by *XRISM*/Resolve of optically thin winds will distinguish between the models and reveal the wind driving mechanism.

7 SUMMARY

We revisit the origin of the density sensitive Fe XXII metastable line in the iconic *Chandra* grating spectrum of GRO J1655−40. This was previously used to rule out an X-ray heated (thermal-radiative) wind in these data, which left magnetic driving as the only viable mechanism. Since magnetic winds should scale with mass and mass accretion rate, this motivated unified models of magnetic winds that spanned both binaries and quasars (F17). We

reanalysed the data using a photoionization code (PION in the SPEX package) which includes the contribution of radiative cascades as well as collisions in populating the metastable level. This reduces the inferred wind density by more than an order of magnitude, removing the requirement for magnetic winds. The derived column is also optically thick, so the source is intrinsically more luminous than observed. We use our state-of-the-art radiation hydrodynamics code to calculate the thermal-radiative wind expected in this source. Our specific simulation goes (marginally) optically thick, and gives a good overall match to all the observed features, both the density derived from the metastable level of Fe XXII, and the range of ion species seen, and their observed velocities. This shows that thermal-radiative winds are not excluded by this unique observation of GRO J1655−40. In fact, given that there no real free parameters barring the inclination, this proof of concept calculation gives strong evidence in favour of an optically thick, thermal-radiative wind as the explanation of these data, though we caution that such extreme winds are very hard to fully simulate.

There could still be magnetic winds in addition to the thermal-radiative wind, and a strong magnetic field might also suppress the thermal wind (Waters & Proga 2018). Hence we also study the MHD wind used in F17 to fit these data. We show that this model also implies that the wind is optically thick, so that the intrinsic luminosity is substantially larger than observed. This means the previous solutions of F17 were not self consistent as the effect of electron scattering reducing the illuminating flux throughout the wind was not included. We include this and show that unlike the thermal-radiative wind, the MHD wind requires additional free parameters of the wind size scale in order to match the ion species seen, even with our lower revised density for Fe XXII.

Thus not only does the thermal-radiative wind give a good fit to GRO J1655−40, the MHD wind does not. This not only removes the *requirement* for magnetic driving, but strongly *disfavours* it as being the origin of the wind seen in this unique observation, though we also show how future observations using high resolution calorimeter data from XRISM/Resolve and Athena/XIFU can easily distinguish thermal-radiative and MHD driving. This means there is no 'special' magnetic field structure, which has self-similarity across the entire mass scale as considered in previous work (F17). Instead, it seems most likely that all the wind features seen in both the stellar and supermassive black holes can be explained by radiation (either from its energy which powers thermal winds via heating and/or its momentum powering UV line and dust driven winds). While the physics of these winds are complex, they can be directly calculated from the observed properties, unlike the magnetic winds which depend on an assumed magnetic field configuration. This provides motivation to tackle the complex astrophysics of radiative winds (e.g. Proga & Kallman 2004; Dorodnitsyn, Kallman & Proga 2016; Nomura & Ohsuga 2017; Matthews et al. 2020; Naddaf, Czerny & Szczerba 2021; Ogawa et al. 2022 and references therein), to make quantitative models of AGN feedback for galaxy formation (e.g. Nomura, Omukai & Ohsuga 2021; Quera-Bofarull et al. 2021).

ACKNOWLEDGEMENTS

This research has made use of data obtained from the Chandra Data Archive, and software provided by the Chandra X-ray Center (CXC). CD and RT acknowledge support from the STFC consolidated grant ST/T000244/1. RT acknowledges computer time on the Cray XC50 at the Center for Computational Astrophysics, National Observatory of Japan. SRON was supported financially by NWO, the Netherlands Organization for Scientific Research. We thank M. Shidatsu for providing their SED data, and K. Fukumura for multiple discussions on the magnetic wind models. We also acknowledge useful discussions with T. Kallman, J. M. Miller, D. Rogantini, S. Zeegers, J. de Plaa, and J. S. Kaastra.

DATA AVAILABILITY

The *Chandra* data are publicly available. The `pion` photoionization code is publicly available as part of the SPEX spectral fitting package. XSTAR code is also publicly available as part of the HEASOFT, X-ray data analysis tool given by NASA. CLOUDY code is also publicly available. Access to the radiation hydrodynamic code is available on request from R.T. (ryota.tomaru@durham.ac.uk).

REFERENCES

Abramowicz M. A., Kluźniak W., 2001, A&A, 374, L19
Beer M. E., Podsiadlowski P., 2002, MNRAS, 331, 351
Begelman M. C., McKee C. F., 1983, ApJ, 271, 89
Blandford R. D., Payne D. G., 1982, MNRAS, 199, 883
Chakravorty S., Lee J. C., Neilsen J., 2013, MNRAS, 436, 560
Contopoulos J., Lovelace R. V. E., 1994, ApJ, 429, 139
Crenshaw D. M., Kraemer S. B., George I. M., 2003, ARA&A, 41, 117
Cunningham C., 1976, ApJ, 208, 534
Del Zanna G., Dere K. P., Young P. R., Landi E., 2021, ApJ, 909, 38
Díaz Trigo M., Boirin L., 2016, Astron. Nachr., 337, 368
Done C., Tomaru R., Takahashi T., 2018, MNRAS, 473, 838
Dorodnitsyn A., Kallman T., Proga D., 2016, ApJ, 819, 115
Dyda S., Dannen R., Waters T., Proga D., 2017, MNRAS, 467, 4161
Ferland G. J., 2003, ARA&A, 41, 517
Fruscione A. et al., 2006, in Silva D. R., Doxsey R. E., eds, Proc. SPIE Conf. Ser. Vol. 6270, Observatory Operations: Strategies, Processes, and Systems. SPIE, Bellingham, p. 62701V
Fukumura K., Kazanas D., Contopoulos I., Behar E., 2010, ApJ, 715, 636
Fukumura K., Kazanas D., Shrader C., Behar E., Tombesi F., Contopoulos I., 2017, Nat. Astron., 1, 0062 (F17)
Greene J., Bailyn C. D., Orosz J. A., 2001, ApJ, 554, 1290
Higginbottom N., Proga D., Knigge C., Long K. S., Matthews J. H., Sim S. A., 2014, ApJ, 789, 19
Higginbottom N., Knigge C., Long K. S., Matthews J. H., Sim S. A., Hewitt H. A., 2018, MNRAS, 479, 3651
Higginbottom N., Knigge C., Long K. S., Matthews J. H., Parkinson E. J., 2019, MNRAS, 484, 4635
Higginbottom N., Knigge C., Sim S. A., Long K. S., Matthews J. H., Hewitt H. A., Parkinson E. J., Mangham S. W., 2020, MNRAS, 492, 5271
Hjellming R. M., Rupen M. P., 1995, Nature, 375, 464
Huenemoerder D. P. et al., 2011, AJ, 141, 129
Kaastra J. S., 2017, A&A, 605, A51
Kaastra J. S., Raassen A. J. J., de Plaa J., Gu L., 2018, SPEX X-ray spectral fitting package
Kallman T., Bautista M., 2001, ApJS, 133, 221
Kallman T. R., Bautista M. A., Goriely S., Mendoza C., Miller J. M., Palmeri P., Quinet P., Raymond J., 2009, ApJ, 701, 865
Kastner S. O., 1993, Space Sci. Rev., 65, 317
Kimura M., Done C., 2019, MNRAS, 482, 626
Laha S., Reynolds C. S., Reeves J., Kriss G., Guainazzi M., Smith R., Veilleux S., Proga D., 2021, Nat. Astron., 5, 13
Lodders K., Palme H., Gail H. P., 2009, Landolt Börnstein, 4B, 712
Luketic S., Proga D., Kallman T. R., Raymond J. C., Miller J. M., 2010, ApJ, 719, 515
Mao J., Kaastra J. S., Mehdipour M., Raassen A. J. J., Gu L., Miller J. M., 2017, A&A, 607, A100
Matthews J. H., Knigge C., Higginbottom N., Long K. S., Sim S. A., Mangham S. W., Parkinson E. J., Hewitt H. A., 2020, MNRAS, 492, 5540
Mauche C. W., Liedahl D. A., Fournier K. B., 2003, ApJ, 588, L101

Mauche C. W., Liedahl D. A., Fournier K. B., 2004, in Vrielmann S., Cropper M., eds, ASP Conf. Ser. Vol. 315, IAU Colloq. 190: Magnetic Cataclysmic Variables. Astron. Soc. Pac., San Francisco, p. 124
Mehdipour M., Kaastra J. S., Kallman T., 2016, A&A, 596, A65
Miller J. M., Raymond J., Fabian A., Steeghs D., Homan J., Reynolds C. S., van der Klis M., Wijnands R., 2006a, Nature, 441, 953
Miller J. M. et al., 2006b, ApJ, 646, 394
Miller J. M., Raymond J., Reynolds C. S., Fabian a. C., Kallman T. R., Homan J., 2008, ApJ, 680, 1359
Miller J. M., Fabian A. C., Kaastra J., Kallman T., King A. L., Proga D., Raymond J., Reynolds C. S., 2015, ApJ, 814, 87
Miller J. M. et al., 2016, ApJ, 821, L9
Naddaf M.-H., Czerny B., Szczerba R., 2021, ApJ, 920, 30
Neilsen J., Rahoui F., Homan J., Buxton M., 2016, ApJ, 822, 20
Nomura M., Ohsuga K., 2017, MNRAS, 465, 2873
Nomura M., Omukai K., Ohsuga K., 2021, MNRAS, 507, 904
Ogawa S., Ueda Y., Wada K., Mizumoto M., 2022, ApJ, 925, 55
Orosz J. A., Remillard R. A., Bailyn C. D., McClintock J. E., 1997, ApJ, 478, L83
Ponti G., Fender R. P., Begelman M. C., Dunn R. J. H., Neilsen J., Coriat M., 2012, MNRAS: Letters, 422, 11
Proga D., Kallman T. R., 2002, ApJ, 20, 455
Proga D., Kallman T. R., 2004, ApJ, 616, 688
Quera-Bofarull A., Done C., Lacey C. G., Nomura M., Ohsuga K., 2021, preprint (arXiv:2111.02742)
Shidatsu M., Done C., Ueda Y., 2016, ApJ, 823, 159
Tomaru R., Done C., Ohsuga K., Nomura M., Takahashi T., 2019, MNRAS, 490, 3098
Tomaru R., Done C., Ohsuga K., Odaka H., Takahashi T., 2020a, MNRAS, 494, 3413
Tomaru R., Done C., Ohsuga K., Odaka H., Takahashi T., 2020b, MNRAS, 497, 4970
Ueda Y., Murakami H., Yamaoka K., Dotani T., Ebisawa K., 2004, ApJ, 609, 325
Waters T., Proga D., 2018, MNRAS, 481, 2628
Woods D. T., Klein R. I., Castor J. I., McKee C. F., Bell J. B., 1996, ApJ, 461, 767

APPENDIX: RADIATION HYDRODYNAMIC SIMULATION

We calculate density, velocity, and temperature distribution of the wind in a 2D (axisymmetric) radiation hydrodynamic simulation, which is the same code as Tomaru et al. (2019, 2020b), but we review it here for completeness. The code requires the SED, its luminosity, and the disc outer radius as input parameters. We take the SED from the simultaneous *RXTE* observation (OBSID:91702-01-19-00) (left in Fig. A1). Using photoionization code CLOUDY, we also calculate

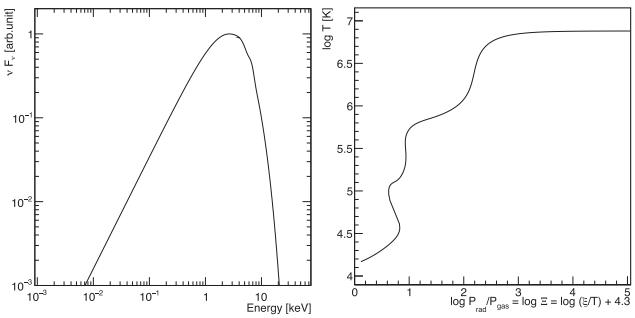

Figure A1. The broadband X-ray continuum (left) and thermal equilibrium curve of photoionized plasma irradiated by that (right).

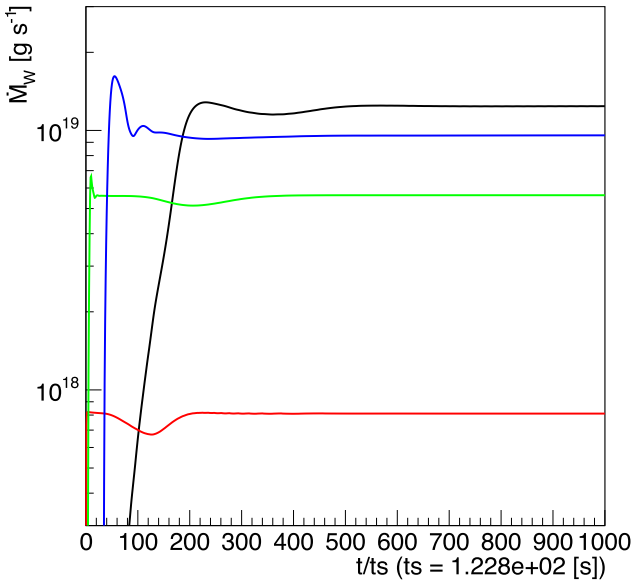

Figure A2. The mass-loss rate at each spherical shells The colours show $0.01 \leq R/R_{\rm IC} \leq 0.038$ (red), $0.038 \leq R/R_{\rm IC} \leq 0.14$ (green), $0.14 \leq R/R_{\rm IC} \leq 0.58$ (blue), and total mass-loss rate at outer boundary (black). It is clear that the simulation has converged after the initial transients.

the thermal equilibrium curve of photoionized plasma irradiated by that SED (right in Fig. A1).

Using CLOUDY and this SED as the input parameter, we calculate radiation heating/cooling and the force multiplier, which is the ratio of effective optical depth to that of electron scattering as functions of ξ and T in optically thin limit. The radiative heating/cooling includes Compton process, free–free, bound–free, free–bound, bound–bound, and force multiplier includes bound–bound and bound–free. We run radiation hydrodynamic simulation by solving the equations in Tomaru et al. (2019). We use spherical polar coordinates, and set the computational domain in R direction as $R_{\rm in} = 0.01R_{\rm IC}$ and $R_{\rm out} = 2R_{\rm IC}$. The radial grid spacing is logarithmic, calculated by

$$R_i = R_{\rm in}(R_{\rm out}/R_{\rm in})^{i/N_R},\ (0 \leq i \leq N_R) \tag{A1}$$

where $N_R = 120$ is the number of radial grid points.

We set the polar angular grid to follow the scale height of the disc model assuming irradiation Cunningham (1976), with $N_\theta = 240$ as the number of grid points defined on the angle from the mid-plane $\alpha_j = \pi/2 - \theta_{{\rm N}_\theta - {\rm j}}$, $(0 \leq j \leq N_\theta)$

$$\alpha_j = \begin{cases} \arctan\left\{ f_d (R_{\rm j}/R_{\rm out})^{2/7} \right\}, & (0 \leq j \leq N_R) \\ \arcsin\left\{ \frac{1.0-\sin(\alpha_{N_R})}{N_\theta - N_R}(j - N_R) + \sin(\alpha_{N_R}) \right\}, & (N_R < j \leq N_\theta) \end{cases} \tag{A2}$$

where $f_d = 1.5 \times 10^{-3} \left(\frac{L}{L_{\rm Edd}}\right)^{1/7} \left(\frac{M_c}{M_\odot}\right)^{-1/7} \left(\frac{R_{\rm out}}{R_{\rm g}}\right)^{2/7}$ is the shape (H/R) of the irradiated disc from Cunningham (1976), as recast in Kimura & Done (2019).

We use outflow boundary conditions for both the inner and outer boundary in the R direction, where the material freely can leave the simulation grid but cannot enter. In θ direction, we use the axially symmetric boundary at the rotational axis of the accretion disc at $\theta = 0$ and reflecting boundary at θ_{N_θ}. At each time step, we update the density at disc surface at $i = j$ as derived from the critical value of the pressure ionization parameter. The complex shape of the heating/cooling equilibrium curve shown in Fig. A1 has

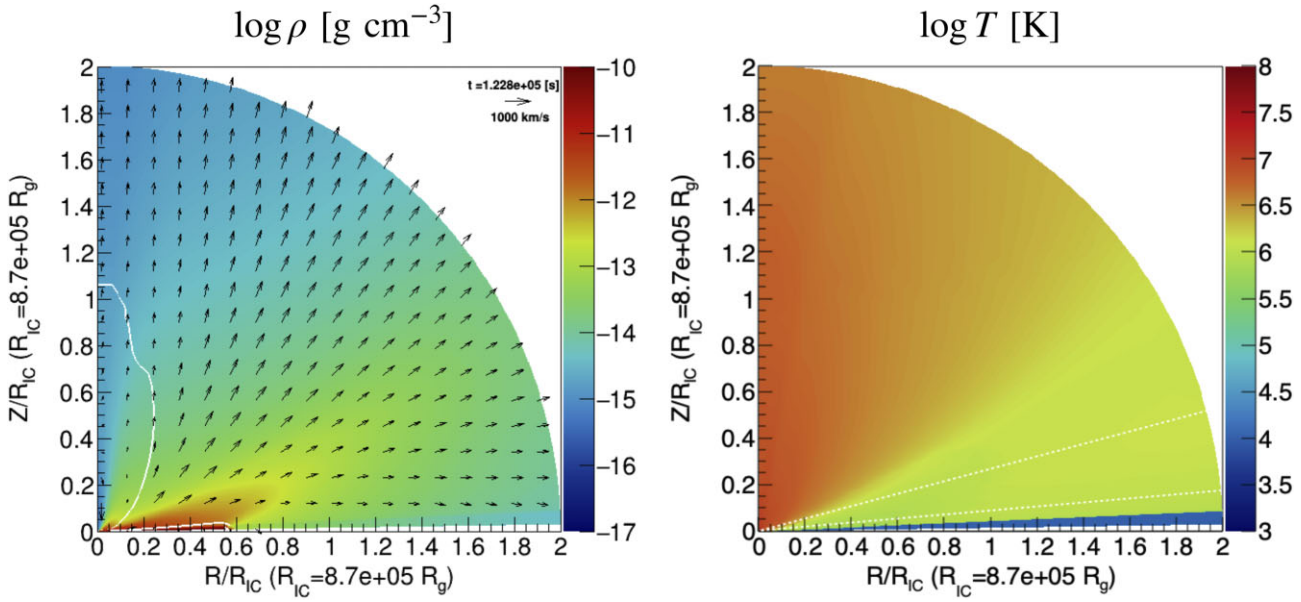

Figure A3. The distributions of density (left) temperature (right) obtained from our radiation hydrodynamic simulation. The white line in left shows the Mach 1 surface. The white dashed line in the right shows the inclination angle of 75° and 85°. The region between these angles is used for the plotting Fig. A5.

multiple instability regions. The first one reached by the radiation going into the photosphere from above is at the end of the warm stable branch, at $\log \Xi_c \sim 0.9$ and $\log T = 5.6$. This corresponds to a standard ionization parameter of $\xi_c \sim 200$, so the material already has substantial soft X-ray opacity, shadowing the regions below, whereas the heating/cooling curves are calculated assuming unattenuated radiation. Thus we use the first instability to determine the base density of the corona $\rho_{\rm bc} = \mu m_{\rm p} L/(\xi_{\rm c} R^2)\exp(-\tau)$, where τ is the integrated optical depth through the wind along a line of sight from the centre to the disc surface, which means the boundary of the disc surface is time dependent (see also Tomaru et al. 2019).

We also assume there is further attenuation of the direct irradiation in an inner static corona region, with $\tau_0 = \exp[2(1-(\alpha/\alpha_{\rm c})^2)]$, where $\alpha_{\rm c} = H_c/R_{\rm ia}$ and $R_{\rm ia}$ is the radius of inner corona given by

$$R_{\rm ia}/R_{\rm IC} = 0.021\left[\frac{T_{\rm IC,8}(L/L_{\rm Edd})}{\Xi_{\rm H,min}0.1}\right]^{1/2} \quad \text{(A3)}$$

(Begelman & McKee 1983) and $H_{\rm c} = [2R^3/R_{\rm IC}]^{1/2}$ is its scale height. The $\Xi_{\rm H,min} = 190$ ($\log \Xi_{\rm H,min} = 2.27$) is the pressure ionization parameter where $T = T_{\rm IC}/2$ on thermal equilibrium curve (right in Fig. A1). This optical depth becomes smaller than unity when R is larger than $0.06R_{\rm IC}$.

As initial conditions in the disc region, $R_i \geq R_j$, we set velocity as $v_R = 0$, $v_\phi = v_K$ and density as $\rho_{\rm bc}$. In the non-disc region, we assume very small density $\rho = 1.0 \times 10^{-30}$ g cm^{-3}, and $T_0 = 1.1 \times 10^7 (R/R_{\rm g})^{-3/4}$ K.

We run the simulation for about 3 sound crossing time $3R_{\rm IC}/c_{\rm IC} = 1.2 \times 10^5$ s. The mass-loss rate of the simulation is converged after 1.5 sound crossing time (Fig. A2). The mass-loss rate is 1.24×10^{19} g s^{-1} $= \dot{M}_{\rm wind}/\dot{M}_{\rm a} = 2.8$.

The analytic thermal wind models predict $\dot{M}_{\rm wind}/\dot{M}_{\rm a} \propto \log[R_{\rm disc}/(0.1R_{\rm IC})]$ for systems with the same $T_{\rm IC}$ and $L/L_{\rm Edd}$ (Woods et al. 1996; Done et al. 2018). This scaling works to compare the total mass loss rate to our previous simulation of the similar SED and luminosity source GX13+1 (Tomaru et al. 2020b), where $\dot{M}_{\rm wind}/\dot{M}_{\rm a} \sim 8$ as the disc in GX13+1 has outer radius of $10R_{\rm IC}$ compared to $0.5R_{\rm IC}$ in GRO J1655−40.

The thermal-radiative wind can in principle be launched from a smaller inner radius than 0.1 $R_{\rm IC}$, because of the strong radiation force, but due to the shadowing of the inner corona (equation A3) out to $R \sim 0.1R_{\rm IC}$, the amount of this inner wind is small. This smaller launching radius by radiation force is also shown in Proga & Kallman (2002), though there are several differences in assumptions which mean that their simulations are not directly comparable to ours.

We plot the final distribution of density and temperature (Fig. A3). These structures are similar to those in our previous simulation of GX 13+1 (Tomaru et al. 2020b) except for detailed parameters such as disc size (which also affects the simulation box size). The white blank region at mid-plane is outside of our simulation box. Fig. A4 shows the distribution of radiation force (left), gas pressure force (middle), centrifugal force by v_ϕ (right), all given as a ratio to the local gravity. This shows that the wind is driven by radiation force and centrifugal force at disc surface, but that gas pressure forces generally dominates at larger radii in the wind. At $R = 0.3R_{\rm IC}$, the radiation force is larger than 0.5, which means the bound-bound and bound-free are significant as well as free-free (electron scattering). This is consistent with a previous simulation (Tomaru et al. 2019) which also showed that electron scattering alone is not sufficient to get the observed velocity.

We also plot the wind properties in $\Xi - T$ space between 75° and 85° with radius (Fig. A5). The wind is converged to the thermal equilibrium curve at large radii, but the inner regions are slightly below this curve due to adiabatic cooling. In the analysis, we calculate iron ion columns as $N_{\rm ion,Fe} = \sum \delta N_{\rm ion,Fe} = \sum f_{\rm ion,Fe}(\xi, T) A_{\rm Fe}\rho/(\mu m_{\rm p})\delta R$, where $f_{\rm ion,Fe}(\xi, T)$ is ion fraction, which is also calculated by CLOUDY, and $A_{\rm Fe} = 3.3 \times 10^{-5}$ is the iron abundance with respect to hydrogen. We also calculate the average velocity weighted by those ion columns as $v_{\rm R,ion} = \sum \delta N_{\rm ion,Fe} v_{\rm R}/N_{\rm ion,Fe}$. These results are given in Fig. 3 in the main paper.

We test that the numerical grid has sufficient resolution by using a smaller $(N_r, N_\theta) = (90, 180)$, and larger $(N_r, N_\theta) = (240, 480)$ grids.

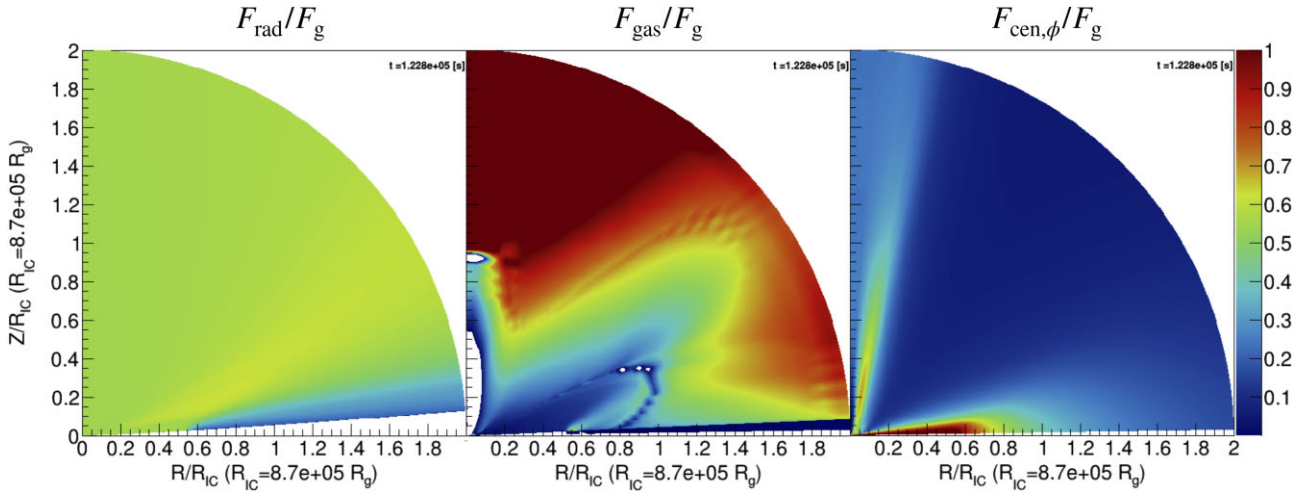

Figure A4. The distribution of radiation force (left), gas pressure force (middle), and centrifugal force (right), all given as a ratio to the local gravitational force. The radiation force is almost zero at high inclination angle with $R > R_{\rm disc}$ since the illumination is attenuated by disc structure.

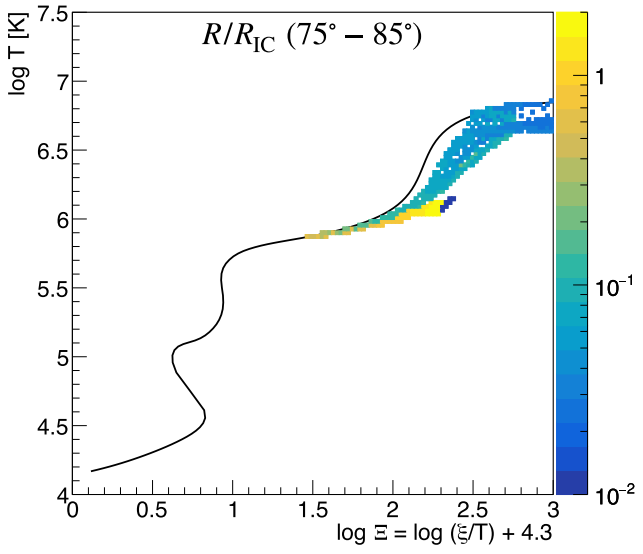

Figure A5. The black line shows the relation between pressure ionization parameter and temperature for the thermal equilibrium curve for optically thin material. The values for the wind material between 75° and 85° are colour coded by their radius. The higher ionized material is located at the inner radius ($\leq 0.2R_{\rm IC}$, blue), the lower ionized material is located at the outer radius ($>0.2R_{\rm IC}$, yellow). Both are below the thermal equilibrium curve due to adiabatic losses.

In the smaller number case, the simulation is not well calculated at larger radius because the larger radius is sparse as grid is logarithmic. But the integral values (velocity and ion columns) are similar to the original simulation because these values are mainly set by the inner region. The higher resolution grid model gives the same result as original model. Thus, we conclude our simulation grid is sufficient to capture the wind properties.

We checked also the impact of the inner boundary condition of the grid. The velocity structure of Fe XXVI at high inclination changes when the inner boundary condition is changed to inflow/outflow instead of just outflow. However, the mass-loss rate and ion columns are almost the same. So, the overall feature of the wind itself is not so different.

This paper has been typeset from a TEX/LATEX file prepared by the author.